IEEE Access
Multidisciplinary | Rapid Review | Open Access Journal

IEEE GEOSCIENCE AND REMOTE SENSING SOCIETY SECTION

Received 14 January 2024, accepted 22 January 2024, date of publication 26 January 2024, date of current version 5 February 2024.

Digital Object Identifier 10.1109/ACCESS.2024.3358812

RESEARCH ARTICLE

Remote Sensing Image Classification Based on Multi-Spectral Cross-Sensor Super-Resolution Combined With Texture Features: A Case Study in the Liaohe Planting Area

HAO HAN[1], ZIYI FENG[1,2,3], WEN DU[1,2,3], SIEN GUO[1], PENG WANG[1], AND TONGYU XU[1,2,3]

[1]College of Information and Electrical Engineering, Shenyang Agricultural University, Shenyang 110866, China
[2]Liaoning Provincial Key Laboratory of Smart Agriculture Technology, Shenyang 110866, China
[3]High-Resolution Earth Observation System, Liaoning Forest and Grass Resources and Environment Remote Sensing Research and Application Center, Shenyang 110866, China

Corresponding author: Tongyu Xu (xutongyu@syau.edu.cn)

This work was supported in part by the Liaoning Provincial Department of Education Project under Grant LJKZ0680.

ABSTRACT High-resolution (HR) optical remote sensing images are typically small in swath and, due to cloud cover, their revisit period, mosaic error, and other problems, it is often infeasible to obtain a large range of remote sensing images for a study area. Meanwhile, low-resolution (LR) satellite images suffer from insufficient spatial and texture information for ground objects. Therefore, classifying a study area with high spatial resolution, large area, and no cloud occlusion using optical remote sensing imagery is very difficult. In recent years, the rapid development of super-resolution reconstruction (SRR) technology has made high-quality spatial resolution reconstruction possible. The SRR of real images is usually accompanied by problems such as sensor spectral range differences, cloud occlusion in the research area, and the SRR algorithm sacrificing a lot of the original information. In this study, with an improved PGGAN, we use only a small number of samples, the wide-swath medium-resolution satellite was restored to the same resolution as the high-resolution satellite, a new method for SRR multi-spectral optical remote sensing image classification based on texture reconstruction information is proposed, and a wide range of high-precision feature classifications are achieved in the study area. In order to solve the problem of spectral distortion in the process of multi-spectral image SRR and the weak generalization of optical remote sensing image ground object classification due to the difference between temporal and spatial features, we combine the idea of ground object classification with texture features obtained after super-resolution reconstruction. We used the support vector machine (SVM) and random forest (RF) classification methods to evaluate the classification effect of each texture spectral feature combination, with the overall accuracy (OA) of the SVM and RF classifiers reaching 98.93% and 98.51%, respectively. The land-use and land-cover (LULC) classification accuracy of the SRR images combined with texture features is much higher than that when directly classifying the original GaoFen-1 and Sentinel-2 images. The obtained results imply that the method of superimposing texture features allows for better classification results in the Liaohe estuary area, providing a new technical idea for the study of LULC classification.

INDEX TERMS Super-resolution, deep learning, generative adversarial network, land use and land cover, multi-spectral remote sensing.

I. INTRODUCTION

As the cornerstone of remote sensing image analysis, remote sensing image feature classification plays a very important role in precision agriculture [1], military reconnaissance, urban land planning [2], and topographic map updating [3]. Crucial challenges in using optical remote sensing imagery for analysis relate to the temporal and spatial resolution, cost, and availability of the data. High-resolution(HR) images have higher resolution, smaller pixels, and richer details, but are

The associate editor coordinating the review of this manuscript and approving it for publication was Stefania Bonafoni.

often not freely available, cloudy weather and stitching errors further limit the practical application of HR optical satellite images.

To solve these problems, special attention is paid to Sentinel-2A/B data, which is an excellent choice for rapid earth observations due to its high temporal resolution (about 5 days). However, the Sentinel-2's red, green, blue, and near Infrared(RGBN) bands have a spatial resolution of only 10 m. Super-resolution reconstruction(SRR) is an image processing technology that restores high-resolution images by applying algorithms to multiple sequential low-resolution(LR) images with complementary information or a single LR image [4]. In order to provide a large area of high-resolution cloud-free imagery (2.5 m per pixel) of the study area, we adopt an SRR method based on style transfer, comprising an improvement of the PGGAN model proposed by NVIDIA in 2017 [5], which is able to achieve 4× cross-sensor super-resolution of Sentinel-2 multi-spectral images.

To date, numerous studies have focused on improving remote sensing image resolution and enhancing the accuracy of various visual tasks by combining image reconstruction methods. In contrast, some existing studies have improved the detection accuracy by combining the SRR and target detection tasks, or the super-resolution and segmentation tasks, in order to improve the segmentation results [6], [7]. However, there have been relatively few studies focused on improving the classification accuracy of remote sensing images. We aim to solve the problem that images cannot be accurately classified after SRR. The first challenge is the limited availability of SRR data sets for specific areas. Although many open-access data sets [8], [9] can establish identification from satellite data, migration from one study area to another site may not be applicable due to differences in ground features and spatial information. Therefore, we focus on collecting a unique data set for SRR and classification evaluation in the Liaohe planting area.

In our study, we demonstrate the possibility of classifying HR reconstructed images, and integrate texture spatial information to compensate for the misclassification of reconstructed images due to differences in spectral information. The use of remote sensing data with a spatial resolution of 10 meters leads to the identification of two or more features with unclear classification boundaries, such that the resolution accuracy is also low. We aim to use free, easily available, and wide-coverage medium-resolution optical remote sensing data—such as those from Sentinel-2A/B—for accurate classification after reconstruction. If associated paired data sets can be obtained, our method can also be applied to classification tasks in other regions. In summary, the key contributions of this paper are as follows:

- We used a modified PGGAN called PGGAN-MSR, which made it more suitable for multispectral remote sensing image SRR in engineering by trimming the generator and adding skip connections, Our method achieved resolution enhancement and good style transfer between different satellite sensors.
- Through a small number of SRR datasets, we have achieved accurate classification of remote sensing images in the study area with a larger width, higher resolution, and no clouds.
- A new classification method based on resolution reconstruction combined with texture features is proposed, including the super-resolution of satellite imagery from different sources. In particular, Sentinel-2 satellite imagery was reconstructed to 2.5 m resolution using GaoFen-1 (GF-1) images.

II. RELATED WORK

A. REMOTE SENSING IMAGE SUPER-RESOLUTION RECONSTRUCTION

1) TRADITIONAL METHODS

Traditional SRR methods for remote sensing images can be divided into three main categories: Frequency domain methods, spatial domain methods, and frequency domain–spatial domain combination methods. Frequency domain methods can be mainly divided into spectrum unaliasing algorithms, recursive least square methods, and so on. As the theoretical premise of such methods is too idealized, making them unable to be effectively applied in many scenarios, this kind of method is no longer a mainstream subject of research. Although spatial domain methods have good flexibility, they involve a lot of factors such as fuzzy motion, optical fuzziness, and other complex loss models. As a result, relevant optimization methods are complicated and the calculation cost is high; thus, they cannot become mainstream methods. Although frequency–spatial [10] combination methods combine the advantages of frequency and spatial domain methods [11], they cannot become mainstream methods due to their high computational complexity, requiring a large amount of computation [12].

2) DEEP LEARNING METHODS

The first image SRR method based on deep learning was proposed by Dong et al. in 2016 [13]. Deep learning methods break the limitations of traditional methods, while also greatly improving the reconstruction effect. First, LR and HR remote sensing images are input into the deep learning method for learning and training, and the mapping relationship between LR and HR remote sensing images is obtained. Then, LR remote sensing images are input into the trained depth model, through which the reconstructed super-resolution remote sensing images are obtained. At present, the most commonly used SRR methods for remote sensing images based on deep learning are based on convolutional neural networks (CNNs) and generative adversarial networks (GANs).

In terms of remote sensing image SRR, the three most commonly used CNN architectures are SRCNN, VDSR [14], and EDSR [15]. These three methods have achieved good results for the SRR of natural images. SRCNN was the first method to apply a CNN for super-resolution. Based on SRCNN,

VDSR introduces a residual network and expands the function of SRCNN, while EDSR is one of the best methods for general image SRR.

A generative adversarial network (GAN) is a deep model that contains at least two modules—a generative model and a discriminant model—through which the mutual game learning of these two models produces high-quality results. An image SRR method based on GAN was first proposed by Ledig et al. [16]. Subsequently, many researchers have used GANs for SRR of optical remote sensing images and designed different module combinations for different super-resolution tasks on remote sensing images. Haut et al. have focused on the generative model and proposed an hourglass-type generation network architecture [17]. The network was trained in an unsupervised manner. The generating network took random noise as input, generated low spatial resolution data through down-sampling, then transmitted it to the up-sampling structure. The model was optimized repeatedly, and finally generated HR pictures. Compared with modern unsupervised SRR methods, their model showed good results on the UC Merced, RSCNN7, and NWPU-RESIS45 data sets, especially when the image was magnified by 4 times. Jiang et al. have proposed an edge enhancement GAN based on a generative adversarial network which consists of two sub-networks: an ultra-dense sub-network (UDSN) and an edge-enhanced sub-network (EESN) [18]. When the UDSN was used for image reconstruction, the reconstruction result appeared sharp and the edges were seriously polluted by noise. Therefore, EESNs were specially designed to enhance the edges by learning a noise mask. Compared with the classical SRCNN, VDSR, and SRGAN methods, the reconstruction effect of this method was greatly improved.

SSR data sets for remote sensing images are typically constructed with respect to specific locations and individual sensors, resulting in limited ability to generalize models between different locations and sensors. Xiong et al. have improved the loss function and network structure of SRGAN, and proposed an improved SRGAN method (ISRGAN) [19]. The ISRGAN method makes the GAN model training more stable and enhances the generalization ability, such that the remote sensing image can be used anywhere and for different sensors once it is trained. Their experimental results indicated that the accuracy of land-cover classification could be significantly improved by using ISRGAN super-resolution reconstruction; in particular, for roads and buildings with high resolution texture, the accuracy was increased by 15%.

B. LAND COVER INFORMATION EXTRACTION COMBINED WITH TEXTURE FEATURES

In terms of land-cover monitoring, remote sensing is mainly used for the extraction and research of land-cover information [20], [21]. In previous research on image information extraction, image spectral information has been mainly used; however, if only the image spectral information is considered, the optical remote sensing image information extraction process may be affected by shadow, noise, atmospheric correction errors, and other factors, having a certain impact on the extraction results. There may also be problems related to ''different objects with the same spectrum''. Therefore, image information extraction through spectral information alone is limited in practice [19]. The emergence of texture features has provided a solution to this problem. As the derivative data of the image, the texture information reveal the spatial variation law and spatial correlation of the grayscale information of the image. Texture features can reflect the spatial structure information of remote sensing images and the spatial distribution characteristics of the image grayscale, and the problem of the ''different objects with the same spectrum'' can be significantly improved through the combination of texture features and spectral features. With the popularization of high spatial resolution remote sensing image applications, the importance of texture has attracted more attention, as the texture features of high-resolution images are clear and complex, and their differences are large. As such, the use of texture features can effectively improve the accuracy of LULC classification.

In the research on land-cover information extraction from remote sensing images combined with texture characteristics, the earliest method of texture analysis was used directly for information extraction; however, the application of this classification method was greatly limited, and its accuracy could not be guaranteed. Some studies have used texture features as a supplement to extract land-cover information from areas with poor multi-spectral data extraction accuracy [22], [23]. These two methods simply used spectral information and texture information, and did not combine the advantages of both for classification. Therefore, the method of combining texture information with spectral information has become a research hotspot. Most commonly, texture information is used as a supplement to synthesize the texture feature image with the original image through band synthesis, followed by directly superimposing the two based on their dimensions, the result of which is a composite image which is used for land-cover classification. Cao et al. have applied texture features for remote sensing image classification in 2004 [24]. Many researchers have conducted inspiring studies, and a large number of applications have emerged. GLCM is one of the most widely used texture features for remote sensing image analysis: by calculating the correlation between two points in the image at certain distances and directions, comprehensive information of the image in terms of direction, amplitude, and speed can be reflected. Wang et al. have plotted Robinia forests using a combination of spectral, spatial, and GLCM texture information from IKONOS images [25]. Godinho et al. have combined the multi-spectral band with a vegetation index and GLCM texture to improve LULC classification [26]. Mananze et al. have developed and tested an automated land-cover mapping method for a study area in Mozambique, which combined the Landsat 7 and 8 multi-spectral bands, a vegetation index, and GLCM texture features [27]. Hasituya has proposed a new

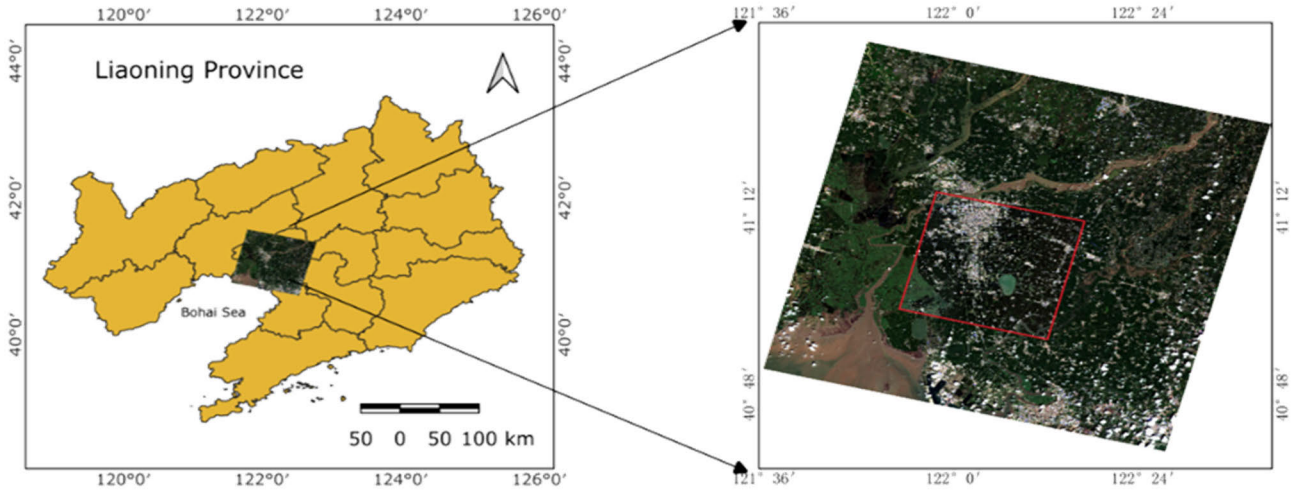

FIGURE 1. Geographic location of the study area within Liaoning Province, China. The red box in the figure shows the range covered by GF-1 with narrow width and high spatial resolution.

scheme combining spectral and texture features to monitor plastic-covered agricultural land, and used an SVM classifier for classification, which obtained a better classification effect [28]. Sarzynski et al. have combined PALSAR-2 and Landsat 8 satellite imagery to map oil palm plantations, using GLCM texture features derived from PALSAR-2 data on the Google Earth Engine (GEE) to improve classification [29]. Przemysław has systematically summarized and compared the effects of different texture analysis methods on land-use classification [30], and concluded that the combination of spectral and GLCM texture information can significantly improve the classification result. Hossein et al. have extracted spectral, texture, and other features from Landsat 8 satellite imagery using the GEE cloud computing platform, in order to accurately classify a study area [31]. Wei et al. have extracted six image features including texture features of GF-6 as feature combinations, then used RF classifiers to accurately classify urban areas [32].

III. MATERIALS AND METHODS

A. STUDY AREA

Rice is the main crop planted on both sides of the Liaohe River. The single-cropping rice area in the Liaohe River Delta [33] is the main rice-producing area in the Liaohe Plain, which is an important japonica rice-producing area in China. It is located in the southwest of Liaoning Province, between 40°39 'N and 41°27' N. Between 121° 25'E and 122° 30'E, the ground is flat and there is plenty of water without mountains. There is enough river water to irrigate the paddy fields. The study area is characterized by a warm temperate continental semi-humid monsoon climate, with sufficient light, four distinct seasons, and slightly alkaline soil, all of which is conducive to the growth and development of rice. The average annual temperature ranges from 8 °C to 11 °C and the average annual precipitation is 618.62 mm. Its estuary is an important wetland conservation area in China, located north of Liaodong Bay and close to the Bohai River estuary, with coordinates latitude of 40°45'–41°10', east longitude of 121°30'–122°00', and covering an area of 223,000 hectares. Located in Panjin City, Liaoning Province, to the southeast of the wetland is the Yingkou urban area, located 35 km from the Panjin urban area. Figure 1 shows the geographic location of the study area.

B. DATASET FOR SR

In this section, we provide a detailed description of the data used to train the GAN model and the image data we used to accurately classify the Liaohe agricultural area.

1) SATELLITE IMAGERY USED IN THE EXPERIMENTS

a: GAOFEN-1

The Gaofen-1 (GF-1) satellite is the first satellite in China's high-resolution Earth observation system [34], providing breakthrough advancements in multiple key technologies such as optical remote sensing combining high spatial resolution, multi-spectrum, and wide land coverage. It has a design life of 5–8 years, and its main parameters and load indicators are provided in Tables 1 and 2.

TABLE 1. The orbit parameters of GF-1 and Sentinel-2.

Orbit parameters	GF-1	Sentinel-2
Type	Sun-synchronous orbit	Sun-synchronous orbit
Altitude	645 km	786 km
Inclination	98.05 degree	98.50 degree
Cycle	41 days	10 days

b: SENTINEL-2

The Sentinel-2(A/B) satellite, which is part of the Global Environment and Security Monitoring program, was launched on June 23, 2015. It carries a multi-spectral imager

which is able to cover 13 spectral bands with different resolution, from visible light and near-infrared to short-wave infrared, with different spatial resolutions and a width of 290 kilometers. Its main parameters and load indicators are provided in Tables 1 and 2.

TABLE 2. Band information for GF-1 and Sentinel-2.

Satellite	Bands	Central wavelength (nm)	Spatial resolution (m)
GF-1	1-PAN	0.45–0.90	2
	2-Blue	0.45–0.52	8
	3-Green	0.52–0.59	
	4-Red	0.63–0.69	
	5-NIR	0.77–0.89	
Sentinel-2	2-Blue	0.490	10
	3-Green	0.560	
	4-Red	0.665	
	8-VNIR	0.835	

2) DATA SET FOR TRAINING

Most standard remote sensing image super-resolution data sets are for scattered land areas and cannot be used for verification of the large-area SRR accuracy in specific research areas. After careful consideration, we combined the PatchesExtraction toolbox provided by Orfeo-toolbox [35] to create the P-W-A (paddy-wetland-August) data set for model training and comparison of the training results. The P-W-A data consisted of sharpened 2.5 m resolution GF-1 images and 10 m resolution Sentinel-2 images for the same date, including buildings, wetlands, rice fields, water bodies, roads, ponds, and other landforms. Samples were collected every 500 meters in the study area to create super-resolution reconstructed images, as shown in Figure 2. A total of 2000 samples were collected, some of which contained cloud images. To achieve 4× super-resolution reconstruction, HR image blocks were cropped to 128 × 128 and LR images were cropped to 32 × 32.

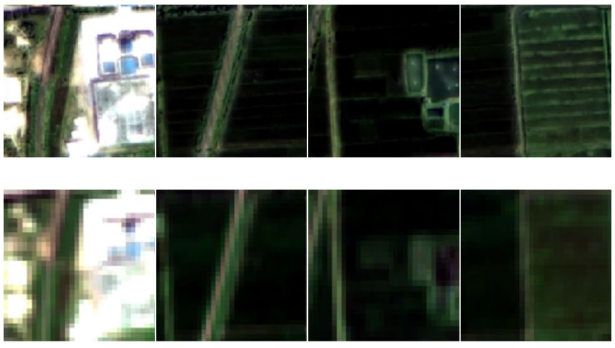

FIGURE 2. Pairs of images produced for training of generative adversarial networks.

C. TECHNOLOGY ROADMAP

We designed a comprehensive experimental plan for this study, consisting of two parts: Multi-spectral remote sensing image SRR based on deep learning, and classification combined with texture features. In the first stage, we achieved 4× upgrading of image resolution. We used the RGBN bands of the down-sampled GF-1 and band-rearranged Sentinel-2 to create LR and HR image pairs with resolutions of 10 m and 2.5 m, respectively. The data sets containing the HR and LR images were used to train a pre-trained PGGAN-MSR model, for which we enlarged the image and increased its resolution from 10 meters to 2.5 meters. The trained model was applied to Sentinel-2 images with a spatial resolution of 10 m to generate a wide high-precision image with a resolution of 2.5 m. Next, we used mature SVM [36] and RF [37] classifiers to accurately classify agricultural planting areas by increasing the spatial information of the texture features.

D. SR METHOD

GAN-based SRR tasks usually utilize two networks: a generator and a discriminator [38], [39]. The generator network converts the input image (i.e., an LR image) into an output image (i.e., a composite HR image). On the other hand, the discriminator inputs two images (i.e., an LR image and an HR image) and produces a signal that indicates the probability that the second image (HR image) is the real image. The goal of a discriminator is to detect ''fake'' (i.e., composite) HR images from real images. Simultaneously, the goal of the generator is to produce an HR image that fools the discriminator by coming close to a real HR image. Next, we introduce PGGAN-MSR, the super-resolution reconstruction method based on PGGAN used in this paper.

In PGGAN [5], the basic methodology is to train the discriminator part at a very low resolution. The discriminator is trained at an original resolution of 4 × 4 and, by adding convolution and up-scaling layers, images at larger resolutions can be constructed. The adaptive growth of the networks makes it easier to learn the styles and spatial features of images with different resolutions. Instead of learning how to map random noise potential vectors to high-resolution images, such as 512 × 512 or 1024 × 1024, the network gradually learns from simple resolutions such as 4 × 4, 8 × 8, and so on. At each resolution, when training the GAN network, there is a ''fade out'' block layer, which helps to smooth the process of upgrading or zooming out between different resolution dimensions. Another major improvement that enables PGGAN to obtain better results is the calculation of losses through the Wasserstein GAN Gradient Penalty (WGGAN-GP) [40]. As the variation between the composite image and the training data set increases, the gradient is severely penalized. This process allows the model to converge faster in the process of high-resolution image generation while maintaining better model accuracy through initial scoring [41], in order to generate more realistic output images.

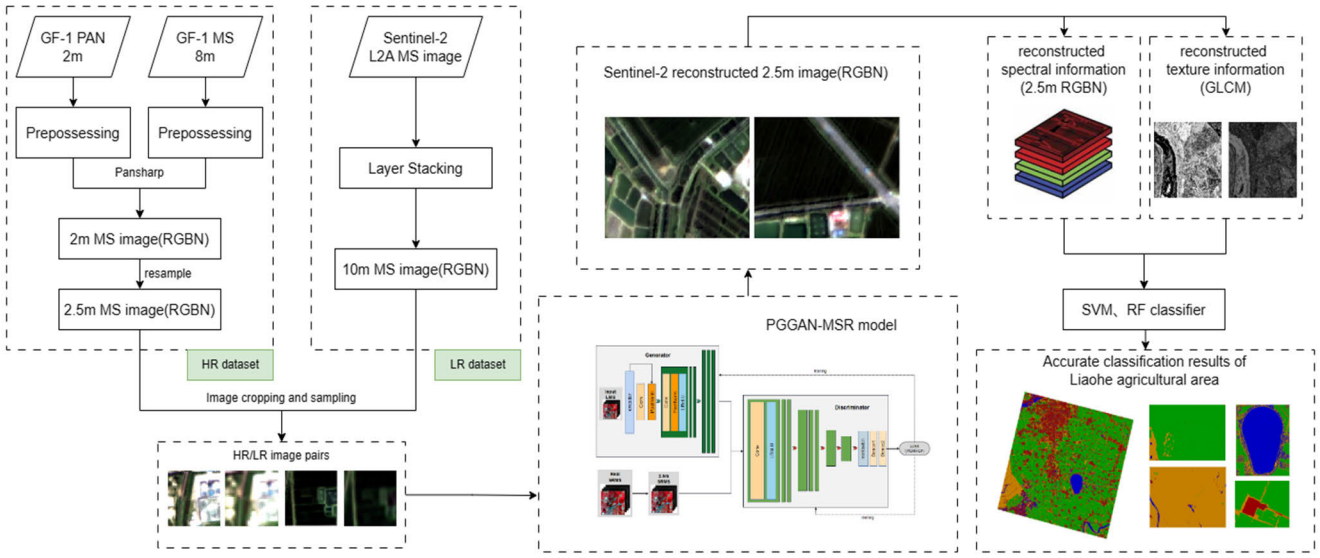

FIGURE 3. Roadmap of the classification experiment.

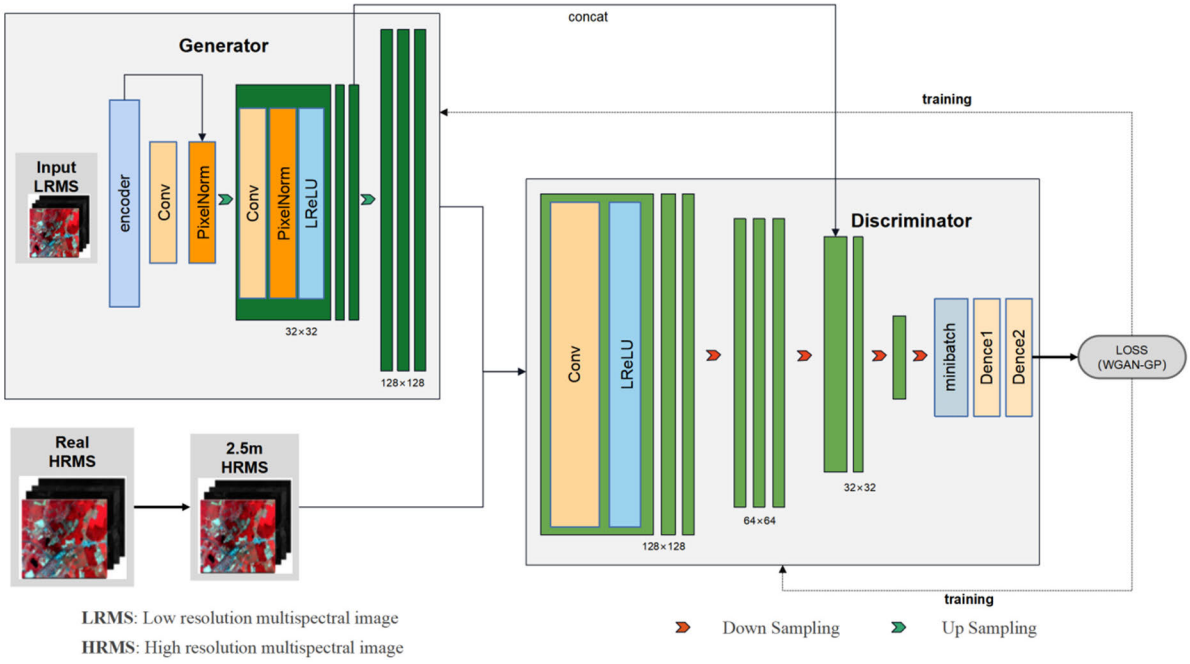

FIGURE 4. Structure diagram of PGGAN-MSR network.

In this paper, PGGAN-MSR, an SRR method for multispectral remote sensing (MSR) images, is proposed based on PGGAN. The model is shown in Figure 4, which can achieve 4× super-resolution; however, with overlay the corresponding up-sample layers, other multiples of resolution reconstruction can be achieved. We added jump connections to enhance the stability of PGGAN during resolution reconstruction training, and reduced the number of layers in the generator, thus decreasing unnecessary computational overhead and enhancing the robustness of the model.

IV. EXPERIMENT

This section describes the various experimental settings and analyzes the test results obtained for all relevant methods.

A. EXPERIMENTAL ENVIRONMENT

The experimental environment platform used in this paper was as follows: NVIDIA Quardo P5000 GPU with CUDA-12.0, CUDNN-8.2.4, TensorFlow-2.8, and Orefeo-ToolBox version 8.1.

B. QUANTITATIVE METRICS

In order to quantitatively evaluate the effect of SRR, we calculated the peak signal-to-noise ratio (PSNR) [42] and structural similarity index measure (SSIM) [43], both of which are commonly used indicators for image adjustment tasks. At the same time, we also calculated the mean square error (RMSE) [44], spectral angle mapper (SAM) [45], and universal quality index (UQI) [46]. In order to effectively process large images, we cropped the validation images of each type of land-cover into equally sized small patches. Then, we averaged the indicators for all four bands to obtain the final value. The higher the value of the PSNR (unit, dB), the better the quality of the reconstructed HR image. The PSNR is calculated according to the following equation:

$$\mathrm{PSNR} = 10 \times \log(255^2/\mathrm{MSE}). \tag{1}$$

SSIM is one of the main evaluation criteria for the correlation between pixels in an image, and has been used as a mainstream image quality evaluation standard in recent years. The structural similarity index measure of the final two images is shown in Equation 2.

where x represents the original image, y represents the SR image, μ_x represents the average brightness of all pixels in the original image, μ_y represents the average brightness of all pixels of the image to be evaluated, σ_x is the standard deviation of pixels in image x, and the constants C_1 and C_2 are used to prevent the denominator data from taking a value of zero.

$$\mathrm{SSIM}(x, y) = \frac{(2\mu_x\mu_y + C_1)(2\sigma_{xy} + C_2)}{(\mu_x^2 + \mu_y^2 + C_1)(\sigma_x^2 + \sigma_y^2 + C_2)} \tag{2}$$

RMSE is one of the most important indicators for evaluating image indicators, reflecting the degree of difference between the two images. Smaller metrics indicate better image quality. The calculation method is as follows, where m and n are the length and width of the image, respectively. In this paper, the average of the four bands is calculated to obtain the final RMSE result.

$$RMSE = \sqrt{\frac{1}{m \times n} \sum^{m \times n} (x_{ij} - y_{ij})^2} \tag{3}$$

The UQI is an indicator, proposed by Wang et al. [44] in 2005, which is used to evaluate image quality. It comprises a combination of correlation loss, luminance distortion, and contrast between images, and is commonly used to evaluate image quality, similarly to PSNR and SSIM.

$$\mathrm{UQI} = \frac{4\sigma_{xy}\overline{x}\,\overline{y}}{(\sigma_x^2 + \sigma_y^2)[(\overline{x})^2 + (\overline{y})^2)} \tag{4}$$

where x and y are the values of the cells in the original image and the SR image, respectively, σ_x and σ_y are the respective variances, and σ_{xy} is the covariance of the pixel values in two images.

In order to compare the spectral deviation of the reconstructed image, we calculated the spectral angle mapper (SAM). The SAM is often used to calculate the similarity between two spectral curves, and its calculation result can be regarded as the cosine angle value of the two sets of data, where a smaller angle indicates a higher similarity. In our work, SAM was calculated as follows:

$$\theta_{\mathrm{SAM}} = \cos^{-1} \frac{y^T x}{(y^T y)^{1/2}(x^T x)^{1/2}}, \tag{5}$$

where y is the spectrum of the original image and x is the corresponding spectrum in the reconstructed image to be evaluated.

LULC having become a popular research topic, numerous result verification methods have emerged, among which the most objective and commonly used method is the confusion matrix. Checking the classification results for accuracy and reliability is of great practical significance, as it not only allows for objective evaluation of the classification results, but also for evaluation of the quality of the source image by comparing multiple classification results. The accuracy of the original image and reconstructed image classification can be evaluated using an error confusion matrix (Confusion Matrix Using Ground Truth ROIs). The indicators mainly include the mapping accuracy, user accuracy (UA), overall accuracy (OA), and Kappa coefficient. We calculated UA and OA for evaluation of the classification accuracy. We used stratified random sampling to calculate OA and UA, seventy percent of the entire datasets were used for training, while thirty percent were used as validation datasets. Some auxiliary datasets such as Google Map and Google Street View were used to collect the sampling datasets.

C. SUPER-RESOLUTION EXPERIMENT RESULTS ON PGGAN-MSR NETWORK

The main idea of PGGAN-MSR is to gradually increase the scale of the generators and discriminators based on PGGAN. The network was initially trained at very low resolution, following which new layers were gradually added to improve the details during training. The details of training are provided in Table 3. This practice not only accelerated the training, but also made the training more stable, improved the clarity of the image in the experimental results, and allowed a better description of the texture features of objects to be obtained. The PGGAN-MSR network based on the P-W-A training set with transfer training achieved a good effect, and the experimental data obtained are detailed in Table 4. We evaluated the reconstruction results using the five indicators mentioned above.

TABLE 3. Parameter settings for training the pre-trained PGGAN-MSR.

Parameter	Value	Parameter	Value
vgg type	vgg19	batch size	4
vgg weight	0.0003	adam	0.0002
L1 weight	200	L2 weight	0.0
LR scale	0.0001	depth	64
HR scale	0.0001	epochs	50

FIGURE 5. Comparison of SR results in large areas. From left to right: S2 original 10 m image, GF-1-pansharp-2.5 m image, bicubic reconstructed sentinel-2 2.5 m image, SRGAN reconstructed sentinel-2 2.5 m image, and PGGAN-MSR reconstructed sentinel-2 2.5 m image.

As shown in Table 4, the overall image reconstruction quality was good. Rice fields and residential areas received higher PSNR scores, while water and rice fields scored relatively better in the SSIM index, which is more in line with human visual evaluation indicators. The root mean square error was low for all feature classes. Rice fields obtained the best SAM results (0.041 degrees), and the SAM values of several other types of features—although not as ideal as those for rice fields—were also within the acceptable limits. The indicators for the entire images were acceptable, and we believe that the reason why they were slightly lower than those for individual features is due to cloud occlusion.

TABLE 4. Verification of accuracy after SRR.

	SSIM↑	PSNR↑	RMSE↓	SAM↓	UIQ↓
Paddy field	0.821	29.833	0.055	0.041	0.362
Wetland	0.732	25.173	0.093	1.444	0.211
Residential area	0.761	32.137	0.057	4.007	0.313
Water (pond)	0.830	26.506	0.047	0.989	0.159
Total	0.801	23.594	0.074	0.030	0.262

The PGGAN-MSR network was employed for SRR of optical remote sensing images. The bit depth of the original image was increased from 24 bits to 32 bits, enhancing the spatial and texture information contained in the object, improving the accuracy of the target detector, and reducing the false and missed detection rates. Compared with the original LR image, the image output by the GAN network presented more obvious texture information and richer spatial information. Figures 5 and 6 show a comparison of the images after SRR. From the figure, we can see that the method in this paper achieves a better visual effect in the work of SRR, the spectrum is closer to the original image, compared with the traditional algorithm and SRGAN, the thin cloud can be removed, and the texture details of the ground object are also well improved.

D. CLASSIFICATION OF SUPER-RESOLUTION RECONSTRUCTED IMAGES COMBINED WITH TEXTURE FEATURES

1) EXTRACTION OF TEXTURE FEATURES

In 1973, Haralick first proposed the GLCM, which is superior to the gray-level run length method and spectral method. The GLCM method describes the spatial structural characteristics and correlations between pixel pairs based on the spatial relationship between image grayscale values. In this work, we used the Co-occurrence module in the ENVI 5.6.3 software to extract eight texture features from the images. These features included mean, variance, homogeneity, contrast, difference, entropy, angular second-order moment, and correlation. Among them, the mean value reflects the change of light and shade of the image, the variance indicates the degree of dispersion of neighboring cells in the image, the homogeneity describes the similarity of the cells within the window, the contrast describes the depth and smoothness of the image texture features, the difference measures the similarity of cell textures within a window, the entropy measures the complexity of the image texture distribution, and the angular second-order moment reflects the regularity and uniformity of the cell distribution [47], [48], as depicted

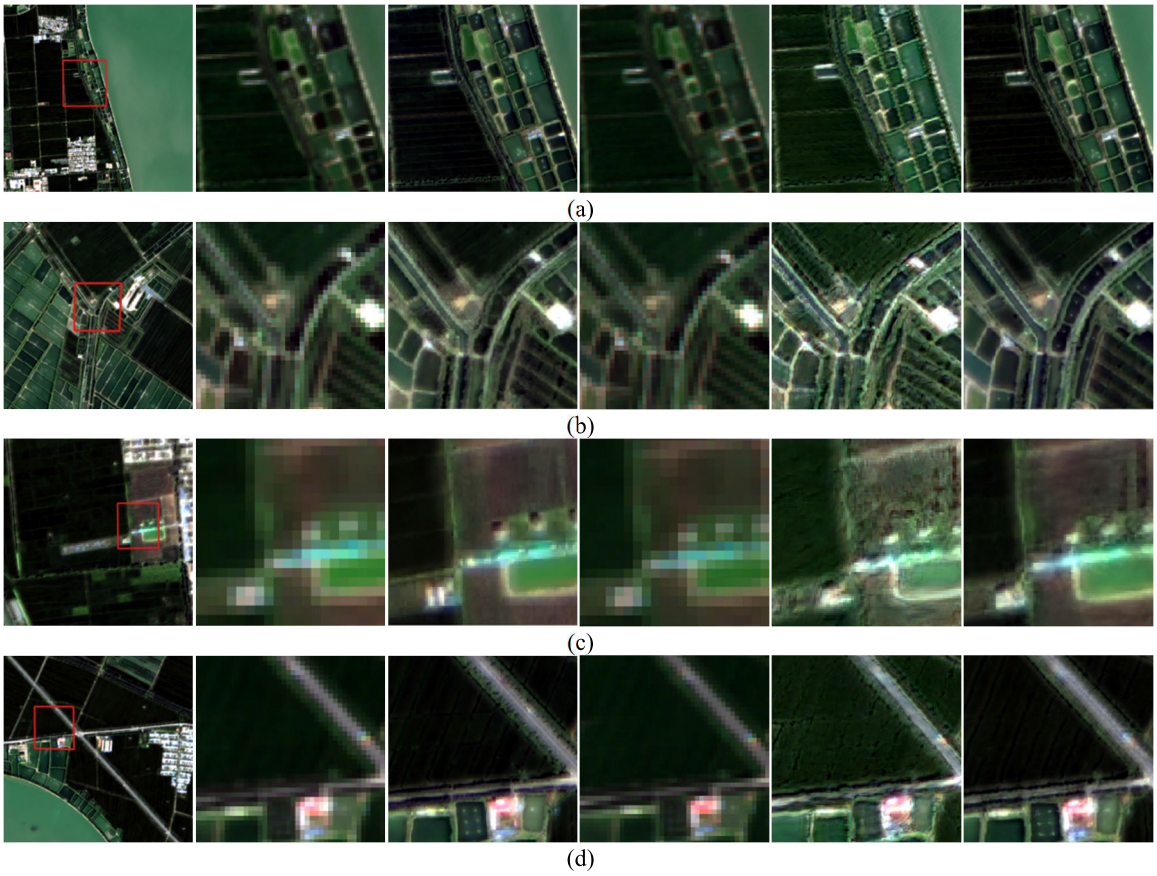

FIGURE 6. Small area comparison. From left to right: schematic diagram of the intercept area, S2 original 10 m image, GF-1-pansharp 2.5 m image, bicubic reconstructed sentinel-2 2.5 m image, SRGAN reconstructed sentinel-2-2.5 m image, and PGGAN-MSR reconstructed sentinel-2-2.5 m image. (a) Ponds and paddy fields; (b) Area with complex features; (c) Soil, trees, and paddy fields; and (d) Paddy fields, roads, and ponds.

in Figure 7. In our experiment, we set the size of the sliding window to 3×3.

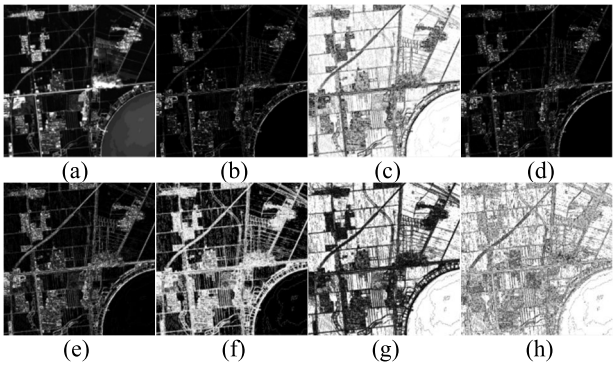

FIGURE 7. Different texture features extracted from SR images in this paper: (a) Mean; (b) Variance; (c) Homogeneity; (d) Contrast; (e) Dissimilarity; (f)Entropy; (g) Second Moment; and (h) Correlation.

2) CLASSIFICATION RESULTS FOR PLANTING AREA IN LIAOHE RIVER BY BLENDING TEXTURE FEATURES

Crops often exhibit similar spectral curves in multi-spectral satellite images during the growing season, which is also known as the ''different objects with the same spectrum'' phenomenon. Moreover, due to the influences of the atmosphere and solar altitude angle, even the same type of ground objects in the same source data may present spectral differences. Additionally, it takes a certain period for the satellite to run over a designated area and, even if it reaches the area, the ground image may not be obtained due to certain weather conditions (e.g., cloud and fog). The spectral characteristics of ground objects will also change due to the time phase of homologous images. At the same time, the phenomenon of ''different objects with the same spectrum'' becomes more obvious due to the differences between sensors when multi-source images are reconstructed. To obtain better classification results, we fused more spatial information in the classification. Specifically, we used the calculated image texture information to assist in the classification, thus reducing the spectral transfer error caused by multi-source sensors.

For this experiment, a reconstructed Sentinel-2 Liaohe planting area image was used for classification. The image acquisition date was August 16, 2022, and the image mainly covered agricultural land, including rice fields, wetlands, water bodies, buildings, roads, and other features. It can be found that rice fields and wetlands in the growing season present similar color and spectral information; however, their texture information significantly differs. Due to the different water quality components of the water surface in agricultural

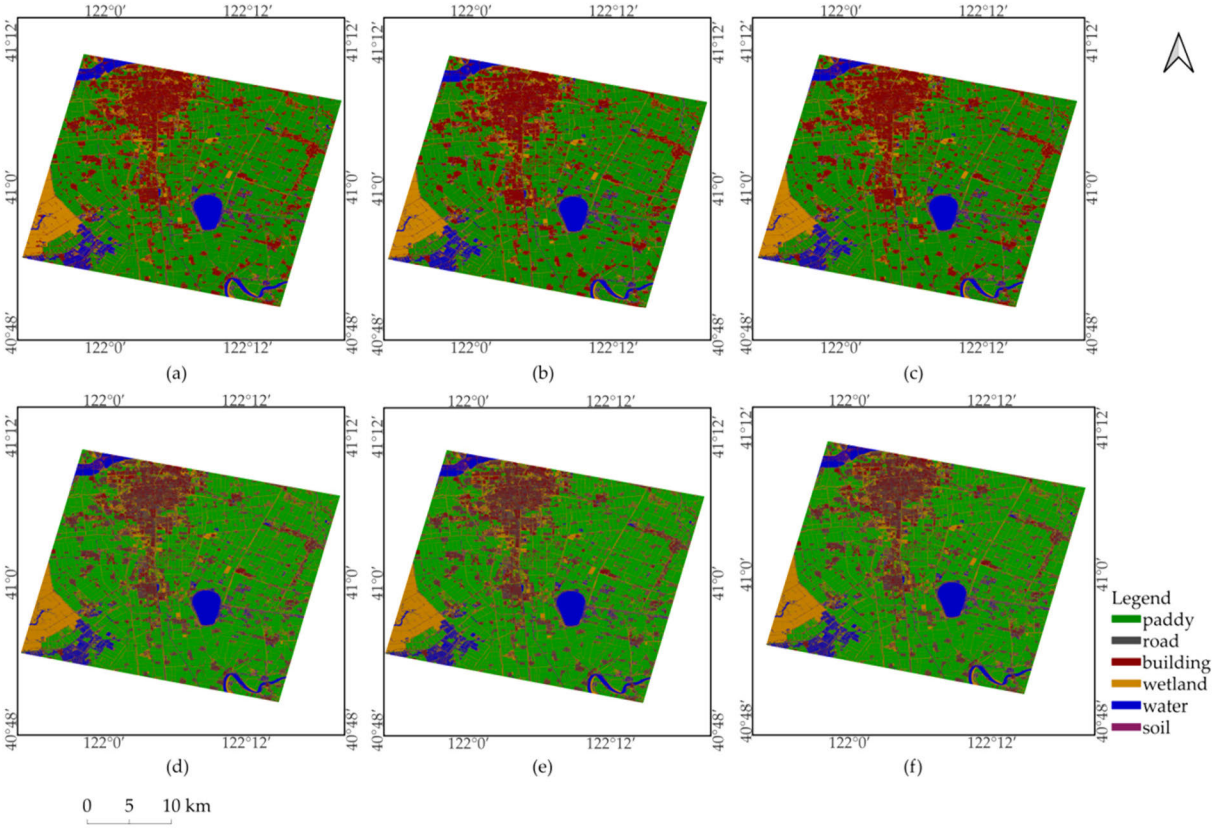

FIGURE 8. Comparison of the classification maps. Classified maps based on SVM algorithm using (a) GF-1; (b) Reconstructed 2.5 m Sentinel-2; (c) Reconstructed 2.5 m Sentinel-2 with texture features, as well as classified maps based on RF algorithm using (d) GF-1; (e) Reconstructed 2.5 m Sentinel-2; and (f) Reconstructed 2.5 m Sentinel-2 with texture features.

planting areas, the spectral reflectance will also vary greatly. Due to the differences in geographical location and soil composition, as well as the complex layout of residential areas, different settlements tend to present different characteristics.

From the qualitative analysis of the classification results, it was concluded that, for the Sentinel-2 reconstruction images, the overall classification effect was better; the basic classification of wetlands, paddy fields, and water bodies was correct; and the main classification of construction land was correct. However, there was some misclassification of construction land and water surfaces, as well as rice fields and wetlands, due to the ''different objects with the same spectrum'' problem. Areas that were misclassified into roads or land due to cloud occlusion in the GF-1 image were improved after SRR. When using the grayscale symbiotic matrix texture, the misclassification of water bodies was greatly improved. As shown in Figure 8, while the rice field itself was misclassified into wetland in the reconstructed image classification, the phenomenon of misclassification was reduced when using the GLCM texture features. Although water and ponds were misclassified as roads in the reconstruction image classification, with the assistance of the GLCM texture, the water surfaces were more accurately identified, indicating that the misalignment between the construction land and water bodies had been significantly improved. The assistance of the grayscale symbiotic matrix texture also inhibited the salt and pepper phenomenon in wetlands, due to the misclassification of cells as rice fields, to a certain extent. Additionally, the use of the grayscale symbiotic matrix texture also significantly enhanced the ability to recognize detailed information and, for small areas of ponds, the classification accuracy was higher. Small ponds in paddy fields were identified as buildings or roads in the original image, and this misclassification phenomenon was more obvious on the reconstructed image. Using the grayscale symbiotic matrix texture, small ponds could be better identified. Figures 9 and 10 compare the details of the RF classifier and SVM classifier [49] classification results.

It is worth noting, from Table 5, that images with textured features added after Sentinel-2 SSR and classified by SVM classifiers achieved the highest producer's accuracy for rice paddy, road, and water classes. The images with textured features added to the results of the RF classifier exhibited the highest classification accuracy in upper rice, water, and land, with Producer's accuracies reaching 98.86%, 98.44%, and 83.73%, respectively.Compared with the original Sentinel-2 and Sentinel-2 2.5 m reconstructed images, adding texture features improved the classification accuracy

TABLE 5. Comparison of the classification accuracy for different images and algorithms.

Image	Classes	Indicator	SVM	RF
Pan-sharpened GF-1	Paddy	Producer's accuracy(%)	98.49	97.96
	Wetland		**99.69**	**99.22**
	Road		55.92	60.12
	Water		95.42	87.96
	Soil		83.81	72.07
	Building		95.86	**95.81**
		OA(%)	96.92	94.95
Original Sentinel-2	Paddy	Producer's accuracy(%)	98.66	97.62
	Wetland		99.40	98.52
	Road		54.40	73.42
	Water		98.59	98.20
	Soil		55.00	71.00
	Building		87.33	91.99
		OA(%)	97.72	97.55
Bicubic Reconstructed Sentinel-2	Paddy	Producer's accuracy(%)	95.16	94.50
	Wetland		99.39	99.01
	Road		**64.69**	79.66
	Water		98.13	98.01
	Soil		60.69	62.26
	Building		77.70	91.56
		OA(%)	96.12	95.98
PGGAN-MSR Reconstructed Sentinel-2	Paddy	Producer's accuracy(%)	99.44	98.85
	Wetland		99.34	98.75
	Road		59.33	**87.47**
	Water		99.28	94.35
	Soil		53.32	78.25
	Building		**97.00**	93.10
		OA(%)	97.86	97.35
PGGAN-MSR Reconstructed Sentinel-2 with GLCM feature	Paddy	Producer's accuracy(%)	**99.62**	**98.86**
	Wetland		99.36	98.98
	Road		61.45	85.36
	Water		**99.42**	**98.44**
	Soil		**67.46**	**83.73**
	Building		95.43	93.57
		OA(%)	**98.93**	**98.51**

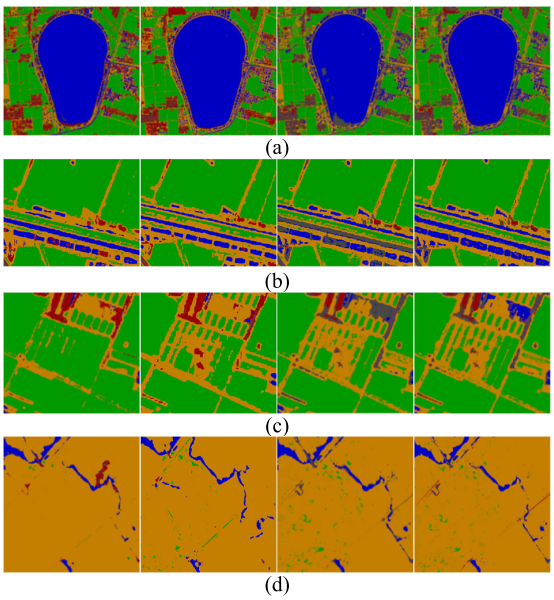

FIGURE 9. Comparison of RF classifier classification results. (a)Lake; (b)Paddy filed and ponds; (c)Paddy field; (d)Wetland. Each group from left to right: GF-1 Pan-sharpened image; Bicubic reconstructed sentinel-2 2.5 m image; PGGAN-MSR reconstructed Sentinel-2 image; PGGAN-MSR reconstructed Sentinel-2 image with GLCM feature.

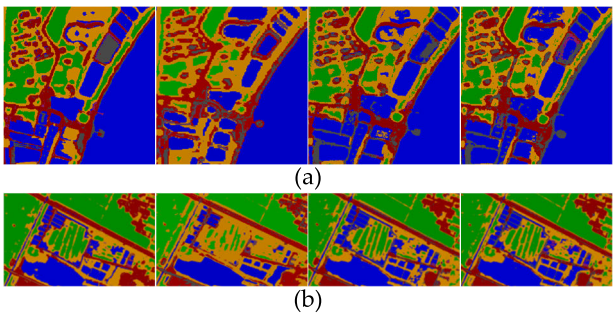

FIGURE 10. Comparison of SVM classifier classification results of Paddy and ponds. From left to right: GF-1 Pan-sharpened image; Bicubic reconstructed sentinel-2 2.5 m image; PGGAN-MSR reconstructed Sentinel-2 image; and PGGAN-MSR reconstructed Sentinel-2 image with GLCM features.

for rice, wetland, road, and water surface classes, and the classification accuracy was the highest for soil, Sentinel-2 image reconstructed by PGGAN-MSR performs better on the rice field classification accuracy than the traditional Bicubic reconstruction method, which we believe is mainly due to the removal of cloud occlusion and the reconstruction method of GAN makes the farmland boundary clearer. Both of the SVM classifier and RF classifier had low overall classification accuracy for roads and soil. Throughout the study, the OA of the SVM classifier was slightly higher than that of the RF classifier; however, this difference was not significant. The SVM classifier had lower classification accuracy than

the RF classifier for roads and soils. Sentinel-2 images with GLCM texture features added after SRR achieved the best OA with both the SVM classifier and RF classifier. This result indicates that the proposed method effectively improved the OA in the study area. Compared with the original image, after reconstruction, the classification accuracy for the water surface class was the most significantly improved; it is also worth mentioning that the OA of the reconstructed Sentinel-2 image and the Sentinel-2 image with texture features added after reconstruction was higher than that on the original GF-1 image.

V. CONCLUSION

In this paper, through the SRR, the high-resolution, large-width, and cloud-free accurate classification of the study area was realized, a new application scenario was proposed in order to classify super-resolution reconstructed images of agricultural areas based on texture information. The method of adding texture features provided more spatial information to the target features to be classified, leading to better classification results. To achieve this, we first studied a cross-sensor optical satellite image super-resolution reconstruction method, and trained the proposed PGGAN-MSR network under the generative adversarial network framework. The traditional PGGAN network only performs style generation of RGB HR images. In this paper, we developed the PGGAN-MSR network based on PGGAN, which gives it the ability to carry out multi-spectral SRR. By reducing the number of layers in the generator, we have reduced unnecessary computational overhead and made it easier for engineering applications. The use of the minibatch standard deviation layer makes spectral migration possible, and the PGGAN-MSR method is closer to the original image than the SRGAN method. Additionally, we used a deeper discriminator network structure, which provided more sufficient training for the discriminator of PGGAN-MSR, the relative average discriminator forces the generator to train on both generated data and real data, which is more conducive to the generation of texture details. The addition of skip connections helped the network to converge better and speed up training. To address the problem that reconstruction cannot be verified in specific large areas, we created a P-W-A data set for the growth season of agricultural areas, which was used for network training and verification.

Next, we extracted texture features from the 2.5 meter resolution images generated by the PGGAN-MSR network as supplementary spatial information. After obtaining the texture information from the reconstructed image, it was superimposed with the original image, and the superimposed image was used as input to the SVM and RF classifiers for supervised classification. Surface object classification experiments were carried out on GF-1 pan-sharpened images, Original Sentinel-2 images, SRR Sentinel-2 images, and SRR Sentinel-2 images with GLCM features. With the addition of texture features, more spatial detail information was added to the original image, allowing better classification results to be obtained for water bodies, paddy fields, and wetland areas; suppression of the salt and pepper noise caused by classification; and significant improvement of the classification accuracy for agricultural areas. The overall classification accuracy under the two classifiers increased by 1.07% and 1.16%, respectively, when compared with only classifying the reconstructed image. A very noteworthy phenomenon observed in this study is that the classification results on the reconstructed image after super-resolution reconstruction were better than when directly classifying the original sharpened GF-1 and Sentinel-2 images, whether or not texture features had been added. This conclusion may provide a new scheme for future practical application research.

In recent years, unsupervised SRR models have been proposed, further research is required to understand the impacts of these models on reconstruction classification tasks. Additionally, in this study, we only tested the $4\times$ SRR effect, while methods based on PGGAN can achieve higher resolution upscaling. The validity of the classification also needs to be verified in larger areas and other features, such as forests [25], deserts, and rocks [50]. Some studies have mentioned the influence of different sizes of sliding windows of GLCM on the classification effect [47], which also needs further study.

REFERENCES

[1] D. J. Mulla, "Twenty five years of remote sensing in precision agriculture: Key advances and remaining knowledge gaps," *Biosyst. Eng.*, vol. 114, no. 4, pp. 358–371, Apr. 2013.

[2] T. Grippa, S. Georganos, S. Zarougui, P. Bognounou, E. Diboulo, Y. Forget, M. Lennert, S. Vanhuysse, N. Mboga, and E. Wolff, "Mapping urban land use at street block level using OpenStreetMap, remote sensing data, and spatial metrics," *ISPRS Int. J. Geo-Inf.*, vol. 7, no. 7, p. 246, Jun. 2018, doi: 10.3390/ijgi7070246.

[3] N. Pierdicca, M. Chini, L. Pulvirenti, and F. Macina, "Integrating physical and topographic information into a fuzzy scheme to map flooded area by SAR," *Sensors*, vol. 8, no. 7, pp. 4151–4164, Jul. 2008, doi: 10.3390/s8074151.

[4] S. C. Park, M. K. Park, and M. G. Kang, "Super-resolution image reconstruction: A technical overview," *IEEE Signal Process. Mag.*, vol. 20, no. 3, pp. 21–36, May 2003, doi: 10.1109/MSP.2003.1203207.

[5] T. Karras, T. Aila, S. Laine, and J. Lehtinen, "Progressive growing of GANs for improved quality, stability, and variation," 2017, *arXiv:1710.10196*.

[6] S. Illarionova, D. Shadrin, I. Shukhratov, K. Evteeva, G. Popandopulo, N. Sotiriadi, I. Oseledets, and E. Burnaev, "Benchmark for building segmentation on up-scaled Sentinel-2 imagery," *Remote Sens.*, vol. 15, no. 9, p. 2347, Apr. 2023, doi: 10.3390/rs15092347.

[7] Y. Wang, H. Wu, L. Shuai, C. Peng, and Z. Yang, "Detection of plane in remote sensing images using super-resolution," *PLoS ONE*, vol. 17, no. 4, Apr. 2022, Art. no. e0265503, doi: 10.1371/journal.pone.0265503.

[8] P. Kowaleczko, T. Tarasiewicz, M. Ziaja, D. Kostrzewa, J. Nalepa, P. Rokita, and M. Kawulok, 2022, "Data for: MuS2: A benchmark for Sentinel-2 multi-image super-resolution," *Harvard Dataverse*, doi: 10.7910/DVN/1JMRAT.

[9] E. Agustsson and R. Timofte, "NTIRE 2017 challenge on single image super-resolution: Dataset and study," in *Proc. IEEE Conf. Comput. Vis. Pattern Recognit. Workshops (CVPRW)*, Honolulu, HI, USA, Jul. 2017, pp. 1122–1131 doi: 10.1109/CVPRW.2017.150.

[10] H. Chavez-Roman and V. Ponomaryov, "Super resolution image generation using wavelet domain interpolation with edge extraction via a sparse representation," *IEEE Geosci. Remote Sens. Lett.*, vol. 11, no. 10, pp. 1777–1781, Oct. 2014, doi: 10.1109/LGRS.2014.2308905.

[11] W. Shen, L. Fang, X. Chen, and H. Xu, "Projection onto convex sets method in space-frequency domain for super resolution," *J. Comput.*, vol. 9, no. 8, pp. 1959–1966, Aug. 2014, doi: 10.4304/jcp.9.8.1959-1966.

[12] G. Anbarjafari and H. Demirel, "Image super resolution based on interpolation of wavelet domain high frequency subbands and the spatial domain input image," *ETRI J.*, vol. 32, no. 3, pp. 390–394, Jun. 2010, doi: 10.4218/etrij.10.0109.0303.

[13] C. Dong, C. C. Loy, K. He, and X. Tang, "Image super-resolution using deep convolutional networks," *IEEE Trans. Pattern Anal. Mach. Intell.*, vol. 38, no. 2, pp. 295–307, Feb. 2016, doi: 10.1109/TPAMI.2015.2439281.

[14] J. Kim, J. K. Lee, and K. M. Lee, "Accurate image super-resolution using very deep convolutional networks," in *Proc. IEEE Conf. Comput. Vis. Pattern Recognit. (CVPR)*, Jun. 2016, pp. 1646–1654 doi: 10.1109/CVPR.2016.182.

[15] B. Lim, S. Son, H. Kim, S. Nah, and K. M. Lee, "Enhanced deep residual networks for single image super-resolution," in *Proc. IEEE Conf. Comput. Vis. Pattern Recognit. Workshops (CVPRW)*, Jul. 2017, pp. 1132–1140 doi: 10.1109/CVPRW.2017.151.

[16] C. Ledig, L. Theis, F. Huszár, J. Caballero, A. Cunningham, A. Acosta, A. Aitken, A. Tejani, J. Totz, Z. Wang, and W. S. Twitter, "Photo-realistic single image super-resolution using a generative adversarial network," in *Proc. IEEE Conf. Comput. Vis. Pattern Recognit. (CVPR)*, Jul. 2017, pp. 105–114 doi: 10.1109/CVPR.2017.19.

[17] J. M. Haut, R. Fernandez-Beltran, M. E. Paoletti, J. Plaza, A. Plaza, and F. Pla, "A new deep generative network for unsupervised remote sensing single-image super-resolution," *IEEE Trans. Geosci. Remote Sens.*, vol. 56, no. 11, pp. 6792–6810, Nov. 2018, doi: 10.1109/TGRS.2018.2843525.

[18] K. Jiang, Z. Wang, P. Yi, G. Wang, T. Lu, and J. Jiang, "Edge-enhanced GAN for remote sensing image superresolution," *IEEE Trans. Geosci. Remote Sens.*, vol. 57, no. 8, pp. 5799–5812, Aug. 2019, doi: 10.1109/TGRS.2019.2902431.

[19] X. M. Zhang, G. J. He, Z. M. Zhang, Y. Peng, and T. F. Long, "Spectral–spatial multi-feature classification of remote sensing big data based on a random forest classifier for land cover mapping," *Cluster Comput.*, vol. 20, no. 3, pp. 2311–2321, Sep. 2017, doi: 10.1007/s10586-017-0950-0.

[20] C. F. Bangs, F. A. Kruse, and C. R. Olsen, "Spectral dependence of texture features integrated with hyperspectral data for area target classification improvement," *Proc. SPIE*, vol. 8743, pp. 636–648, May 2013, doi: 10.1117/12.2015201.

[21] G. Cheng, X. Xie, J. Han, L. Guo, and G.-S. Xia, "Remote sensing image scene classification meets deep learning: Challenges, methods, benchmarks, and opportunities," *IEEE J. Sel. Topics Appl. Earth Observ. Remote Sens.*, vol. 13, pp. 3735–3756, 2020, doi: 10.1109/JSTARS.2020.3005403.

[22] B. Zhang, C. Wang, Y. Shen, and Y. Liu, "Fully connected conditional random fields for high-resolution remote sensing land use/land cover classification with convolutional neural networks," *Remote Sens.*, vol. 10, no. 12, p. 1889, Nov. 2018, doi: 10.3390/rs10121889.

[23] R. Seifi Majdar and H. Ghassemian, "A probabilistic SVM approach for hyperspectral image classification using spectral and texture features," *Int. J. Remote Sens.*, vol. 38, no. 15, pp. 4265–4284, Aug. 2017, doi: 10.1080/01431161.2017.1317941.

[24] W. Cao, T.-Q. Peng, and B.-C. Li, "A remote sensing image classification method using color and texture feature," in *Advances in Neural Networks—ISNN* (Lecture Notes in Computer Science), F.-L. Yin, J. Wang, and C. Guo, Eds. Berlin, Germany: Springer, 2004, pp. 965–970, doi: 10.1007/978-3-540-28647-9_159.

[25] H. Wang, Y. Zhao, R. Pu, and Z. Zhang, "Mapping robinia pseudoacacia forest health conditions by using combined spectral, spatial, and textural information extracted from IKONOS imagery and random forest classifier," *Remote Sens.*, vol. 7, no. 7, pp. 9020–9044, Jul. 2015, doi: 10.3390/rs70709020.

[26] S. Godinho, N. Guiomar, and A. Gil, "Estimating tree canopy cover percentage in a Mediterranean silvopastoral systems using Sentinel-2A imagery and the stochastic gradient boosting algorithm," *Int. J. Remote Sens.*, vol. 39, no. 14, pp. 4640–4662, Aug. 2018, doi: 10.1080/01431161.2017.1399480.

[27] S. Mananze, I. Pôças, and M. Cunha, "Mapping and assessing the dynamics of shifting agricultural landscapes using Google Earth Engine cloud computing, a case study in Mozambique," *Remote Sens.*, vol. 12, no. 8, p. 1279, Apr. 2020, doi: 10.3390/rs12081279.

[28] Hasituya, Z. Chen, L. Wang, W. Wu, Z. Jiang, and H. Li, "Monitoring plastic-mulched farmland by Landsat-8 OLI imagery using spectral and textural features," *Remote Sens.*, vol. 8, no. 4, p. 353, Apr. 2016, doi: 10.3390/rs8040353.

[29] T. Sarzynski, X. Giam, L. Carrasco, and J. S. H. Lee, "Combining radar and optical imagery to map oil palm plantations in Sumatra, Indonesia, using the Google Earth Engine," *Remote Sens.*, vol. 12, no. 7, p. 1220, Apr. 2020, doi: 10.3390/rs12071220.

[30] P. Kupidura, "The comparison of different methods of texture analysis for their efficacy for land use classification in satellite imagery," *Remote Sens.*, vol. 11, no. 10, p. 1233, May 2019, doi: 10.3390/rs11101233.

[31] H. Shafizadeh-Moghadam, M. Khazaei, S. K. Alavipanah, and Q. Weng, "Google Earth Engine for large-scale land use and land cover mapping: An object-based classification approach using spectral, textural and topographical factors," *GIScience Remote Sens.*, vol. 58, no. 6, pp. 914–928, Aug. 2021, doi: 10.1080/15481603.2021.1947623.

[32] X. Wei, W. Zhang, Z. Zhang, H. Huang, and L. Meng, "Urban land use land cover classification based on GF-6 satellite imagery and multi-feature optimization," *Geocarto Int.*, vol. 38, no. 1, Dec. 2023, Art. no. 2236579, doi: 10.1080/10106049.2023.2236579.

[33] L. He, C. Xue, S. Ye, E. A. Laws, H. Yuan, S. Yang, and X. Du, "Holocene evolution of the Liaohe Delta, a tide-dominated delta formed by multiple rivers in Northeast China," *J. Asian Earth Sci.*, vol. 152, pp. 52–68, Feb. 2018, doi: 10.1016/j.jseaes.2017.11.035.

[34] Q.-B. Zhou, Q.-Y. Yu, J. Liu, W.-B. Wu, and H.-J. Tang, "Perspective of Chinese GF-1 high-resolution satellite data in agricultural remote sensing monitoring," *J. Integrative Agricult.*, vol. 16, no. 2, pp. 242–251, Feb. 2017.

[35] M. Grizonnet, J. Michel, V. Poughon, J. Inglada, M. Savinaud, and R. Cresson, "Orfeo ToolBox: Open source processing of remote sensing images," *Open Geospatial Data, Softw. Standards*, vol. 2, no. 1, p. 15, Jun. 2017, doi: 10.1186/s40965-017-0031-6.

[36] G. Mountrakis, J. Im, and C. Ogole, "Support vector machines in remote sensing: A review," *ISPRS J. Photogramm. Remote Sens.*, vol. 66, no. 3, pp. 247–259, May 2011, doi: 10.1016/j.isprsjprs.2010.11.001.

[37] M. Belgiu and L. Drăguţ, "Random forest in remote sensing: A review of applications and future directions," *ISPRS J. Photogramm. Remote Sens.*, vol. 114, pp. 24–31, Apr. 2016.

[38] K. Hayat, "Multimedia super-resolution via deep learning: A survey," *Digit. Signal Process.*, vol. 81, pp. 198–217, Oct. 2018, doi: 10.1016/j.dsp.2018.07.005.

[39] S.-W. Park, J.-S. Ko, J.-H. Huh, and J.-C. Kim, "Review on generative adversarial networks: Focusing on computer vision and its applications," *Electronics*, vol. 10, no. 10, p. 1216, May 2021, doi: 10.3390/electronics10101216.

[40] I. Gulrajani, F. Ahmed, M. Arjovsky, V. Dumoulin, and A. Courville, "Improved training of Wasserstein GANs," 2017, *arXiv:1704.00028*.

[41] T. Salimans and D. P. Kingma, "Weight normalization: A simple reparameterization to accelerate training of deep neural networks," 2016, *arXiv:1602.07868*.

[42] A. Hore and D. Ziou, "Image quality metrics: PSNR vs. SSIM," in *Proc. 20th Int. Conf. Pattern Recognit.*, Aug. 2010, pp. 2366–2369, doi: 10.1109/ICPR.2010.579.

[43] Z. Wang, A. C. Bovik, H. R. Sheikh, and E. P. Simoncelli, "Image quality assessment: From error visibility to structural similarity," *IEEE Trans. Image Process.*, vol. 13, no. 4, pp. 600–612, Apr. 2004, doi: 10.1109/TIP.2003.819861.

[44] R. M. Ezzeldeen, H. H. Ramadan, T. M. Nazmy, M. A. Yehia, and M. S. Abdel-Wahab, "Comparative study for image registration techniques of remote sensing images," *Egyptian J. Remote Sens. Space Sci.*, vol. 13, no. 1, pp. 31–36, Jun. 2010, doi: 10.1016/j.ejrs.2010.07.004.

[45] X. Zhang and P. Li, "Lithological mapping from hyperspectral data by improved use of spectral angle mapper," *Int. J. Appl. Earth Observ. Geoinf.*, vol. 31, pp. 95–109, Sep. 2014, doi: 10.1016/j.jag.2014.03.007.

[46] Z. Wang and A. C. Bovik, "A universal image quality index," *IEEE Signal Process. Lett.*, vol. 9, no. 3, pp. 81–84, Aug. 2002, doi: 10.1109/97.995823.

[47] X. Zhang, J. Cui, W. Wang, and C. Lin, "A study for texture feature extraction of high-resolution satellite images based on a direction measure and gray level co-occurrence matrix fusion algorithm," *Sensors*, vol. 17, no. 7, p. 1474, Jun. 2017, doi: 10.3390/s17071474.

[48] A. Adhikari, R. D. Garg, S. K. Pundir, and A. Singhal, "Delineation of agricultural fields in arid regions from Worldview-2 datasets based on image textural properties," *Environ. Monitor. Assessment*, vol. 195, no. 5, p. 605, Apr. 2023, doi: 10.1007/s10661-023-11115-x.

[49] M. Sheykhmousa, M. Mahdianpari, H. Ghanbari, F. Mohammadimanesh, P. Ghamisi, and S. Homayouni, "Support vector machine versus random forest for remote sensing image classification: A meta-analysis and systematic review," *IEEE J. Sel. Topics Appl. Earth Observ. Remote Sens.*, vol. 13, pp. 6308–6325, 2020, doi: 10.1109/JSTARS.2020.3026724.

[50] G. Zhou, W. Chen, X. Qin, J. Li, and L. Wang, "Lithological unit classification based on geological knowledge-guided deep learning framework for optical stereo mapping satellite imagery," *IEEE Trans. Geosci. Remote Sens.*, vol. 61, pp. 1–16, 2023, doi: 10.1109/TGRS.2023.3327774.

HAO HAN was born in Shenyang, China, in 1997. He received the B.S. and M.S. degrees from the School of Geomatics, Liaoning Technical University, Fuxin, China. He is currently pursuing the Ph.D. degree with the College of Information and Electrical Engineering, Shenyang Agricultural University, Shenyang. His research interests include remote sensing, image processing, and computer vision.

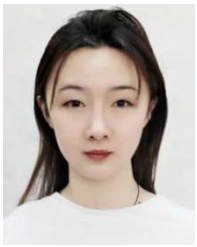

ZIYI FENG was born in Shenyang, China, in 1991. She received the B.S. and M.S. degrees from the School of Computer Science and Engineering, Northeastern University (NEU), and the Ph.D. degree from the College of Water Conservancy, Shenyang Agricultural University, Shenyang, in 2022.

She is currently a Lecturer with the College of Information and Electrical Engineering, Shenyang Agricultural University. Her research interests include satellite remote sensing, remote sensing quantitative retrieval, image fusion, and image super-resolution.

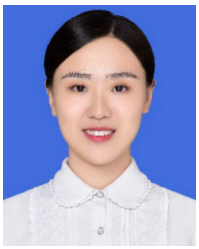

WEN DU received the B.S., M.S., and Ph.D. degrees from the College of Information and Electrical Engineering, Shenyang Agricultural University, Shenyang, China, in 2014 and 2018, respectively.

She is currently a Lecturer with the College of Information and Electrical Engineering, Shenyang Agricultural University. Her research interests include remote sensing and carbon neutrality.

SIEN GUO was born in Chaoyang, Liaoning, China, in 1998. She received the B.S. degree in information and electrical engineering from Shenyang Agricultural University, Shenyang, China, where she is currently pursuing the M.S. degree in information and electronic engineering. Her research interest includes remote sensing land classification.

PENG WANG is currently pursuing the M.S. degree with the College of Information and Electrical Engineering, Shenyang Agricultural University, Shenyang, China. His research interests include agricultural remote sensing and remote sensing image classification.

TONGYU XU received the B.S. degree from Xidian University, Xi'an, China, in 1990, the M.S. degree from the Shenyang Institute of Technology, Shenyang, China, and the Ph.D. degree from Shenyang Agricultural University, Shenyang, in 2006.

From 2005 to 2006, he was a Research Assistant with the School of Electronic Information and Electrical Engineering, Shanghai Jiao Tong University, China. He is currently the Director of the Liaoning Provincial Agricultural Information Engineering Technology Research Center, the Director of the Chinese Society of Agricultural Engineering, and the Vice Chairperson of the Agricultural Aviation Branch of Chinese Society of Agricultural Engineering. His research interests include agricultural remote sensing, precision agriculture, crop phenotypic information acquisition, and analysis.